Water Reuse

© 2022 The Authors

Water Reuse Vol 12 No 2, 242 doi: 10.2166/wrd.2022.102

Continuous and efficient oil/water separation by special wettability granular filter media

Zhang Hongwei[a,b], Qi Junye[a,c], Che Yinglong[a], Man Shide[a], Liu Jianlin[d] and Wei Bigui[a,b,*]

[a] School of Environmental and Municipal Engineering, Lanzhou Jiaotong University, Lanzhou 730070, China
[b] Key Laboratory of Yellow River Water Environment in Gansu Province, Lanzhou 730070, China
[c] CCCC-SHEC Engineering Design & Research Institute, Xi'an 710065, China
[d] Beijing General Municipal Engineering Design & Research Institute Co., Ltd, Beijing, China
*Corresponding author. E-mail: weibg@mail.lzjtu.cn

ABSTRACT

To improve the separation efficiency of the oil/water mixture and simplify the separation process, a superhydrophilic/underwater superoleophobic quartz sand filter media (PR@QS) was prepared by coating potato residue onto the quartz sand surface, and an oil/water mixture separator containing two horizontally placed filter columns and one inlet chamber was proposed. One filter column was filled with the PR@QS, and the other column was filled with the superhydrophobic/superoleophilic quartz sand filter media. The experimental results showed that the separation efficiencies of five kinds of oil/water mixtures (petroleum ether, engine oil, diesel oil, cyclohexane, and methylene chloride) were up to 99.4%. Except for engine oil, the hydraulic conductivities of the other four oils and water are all greater than 3.5 m/h. When the filter layer is invaded by the lyophobic liquid, its filtration performance can be restored by backwashing. In summary, the separator can separate oil/water mixtures continuously and efficiently without filter contamination. Therefore, it has a broad prospect for practical application.

Key words: granular filter media, oil/water mixture separation, special wettability, superhydrophilic/underwater superoleophobic, superhydrophobic/superoleophilic

HIGHLIGHTS

- An oil/water separator consisting of two filter columns filled with two opposite superwettable granular filter media is proposed.
- The separation efficiencies for different oil/water mixtures are higher than 99.4%.
- The separation performance of the separator can be recovered by backwashing.
- The separator can continuously and efficiently separate oil/water mixtures, and it is easy to operate.

GRAPHICAL ABSTRACT

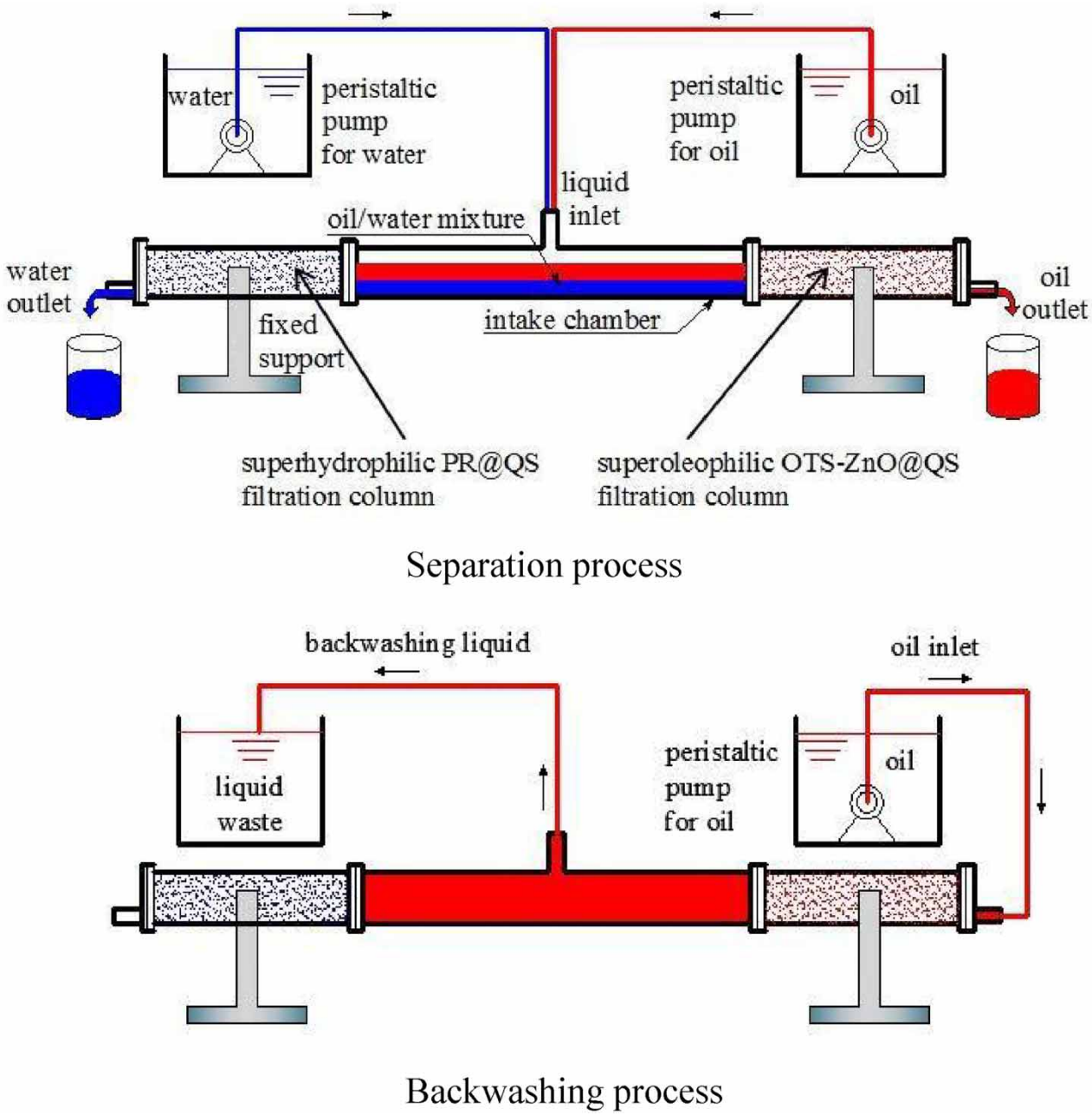

1. INTRODUCTION

Oily wastewater is a kind of industrial wastewater with a large volume and wide range. It mainly comes from the food, textile, petroleum, natural gas, petrochemical, and metal processing industries (Shannon *et al.* 2008). Without effective treatment, oily wastewater will cause serious harm to the environment and human health (Kintisch 2010). Traditional oil/water separation technology includes gravity separation (Hafiz *et al.* 2005), coagulation (Zaroual *et al.* 2006; Calvo *et al.* 2010), skimming (Song *et al.* 2015), flotation (Moosai & Dawe 2003), membrane separation (Tanudjaja *et al.* 2019), adsorption method (Pintor *et al.* 2016), and so on. However, these separation technologies have problems, such as low separation efficiencies, high energy consumption, complicated operational processes, and easy secondary pollution (Zhang *et al.* 2013). Therefore,

more efficient and low-energy consumption oil/water separation technology has become an issue of extensive concern (Li *et al.* 2017; Lian *et al.* 2018; Du *et al.* 2019).

In recent years, special wettability materials have been widely researched (Wang *et al.* 2015). Because the surface tensions of oil and water are different, the wettability of oil and water on the same solid surface may also be different. Based on this feature, some researchers have developed oil/water separation materials with special wettability, such as selective filtration membranes and three-dimensional adsorption materials (Wang *et al.* 2016). The substrates of the selective filtration membranes include iron mesh (Cheng *et al.* 2017), stainless mesh (Jiang *et al.* 2019; Shang *et al.* 2019; Tang *et al.* 2019; Tian *et al.* 2019), copper mesh (Tudu & Kumar 2019; Wang & Liu 2020; Yin *et al.* 2020a), nickel mesh (Yin *et al.* 2020b), aluminum mesh (Zhang *et al.* 2019), commercial fabrics (Yao *et al.* 2019; Meng *et al.* 2020), ethylene terephthalate nonwoven fabric (Yagoub *et al.* 2019), polyvinylidene difluoride (Obaid *et al.* 2017), and so on. The selective filtration membrane allows lyophilic liquid to pass through the membrane hole and prevents the lyophobic liquid from passing through to achieve oil/water separation. Selective filtration has the advantage of high separation efficiency, but the membrane hole is small, usually at the nanometer/micron level; as a result, the membrane flux is small, and the separation process even requires additional pressure. In addition, once the membrane hole is contaminated, it is difficult to clean. The substrates of the three-dimensional adsorption materials include fibers (Li *et al.* 2014; Zang *et al.* 2015), sponges (Ge *et al.* 2014; Ge *et al.* 2015), cotton (Cheng *et al.* 2019), filter paper (Du *et al.* 2014), and so on. The separation method is as follows: first, the adsorption material is immersed in the oil/water mixture, and then, the adsorption material is removed after the lyophilic liquid is adsorbed. This technology also has a great separation efficiency. To reuse the adsorption material, the adsorbed lyophilic liquid needs to be extruded by external forces, such as extrusion, so it has the disadvantage of a complicated operational process. These shortcomings hinder the practical application of selective filtration membranes and three-dimensional adsorption materials.

To overcome these shortcomings, we chose a hard granular filter medium as the substrate, modified it into a special wettability filter medium, and packed it into the filter column for oil/water separation. The filter layer allows lyophilic liquid to flow through the porous channel and intercepts lyophobic liquid. When the filter layer is polluted by the lyophobic liquid, it can be backwashed. Therefore, the operation of the oil/water separation process is very simple. The oil/water mixture involves two liquid phases, namely the water phase and the oil phase. If only one special wettability filter media is used for oil/water separation, the lyophobic liquid will accumulate in the separator, thus blocking the lyophilic liquid from the filter media; as a result, the separation process cannot be continued. For those reasons, we developed a separator, which has two filtration columns, one column packed with superhydrophilic and underwater superoleophobic filter media that allows water to pass through but not oil, and another column packed with superhydrophobic and superoleophilic filter media that allows oil to pass through but not water. Consequently, this separator can separate oil/water mixtures continuously.

Here, the two special wettability granular filter media mentioned above were fabricated using quartz sand as the substrate. Quartz sand is widely used in water treatment because of its high hardness, good stability, and low price (Liu *et al.* 2018a). We have studied the superhydrophobic and superoleophilic quartz sand filter media in an earlier stage (Liu *et al.* 2018b) and directly adopted the same fabrication method in this paper. For superhydrophilic and underwater superoleophobic media, the modifiers mainly include hydrogel (Teng *et al.* 2014), polymer reagents (Yang *et al.* 2015), ZnO nanoparticles (Budnyak *et al.* 2015), graphene oxide (Huang *et al.* 2015), and agro-waste. Because of its advantages, such as its ease of acquisition, large quantity, and low cost, agro-waste has attracted extensive attention from researchers in the field of environmental engineering and science in recent years. For example, Jing *et al.* (2019) using corn bracts, prepared biomass carbon (BC) aerogels with large specific surface areas and superhydrophobicity. The BC aerogels exhibited an extremely high absorption capacity and excellent reusability for oil and could be used to separate oil from water. Jamalludin *et al.* (2019) prepared a hybrid green ceramic membrane using agricultural-sugarcane bagasse waste for the adsorbent/separation of real oily wastewater. Potato residue is a kind of waste produced in the food processing industry. Potato residue is an ideal choice for designing new underwater superoleophobic materials because it contains a large amount of hydrophilic hydrogen bonding. Therefore, we fabricated superhydrophilic and underwater superoleophobic quartz sand filter media by coating potato residue on the quartz sand surface.

This paper studies the separation performance of the separator, including the separation efficiency, intrusion pressure, hydraulic conductivity, backwash performance, and so on. The results show that the separator can separate oil/water mixtures continuously and efficiently and that its separation efficiency is more than 99.4%.

2. EXPERIMENT

2.1. Experimental materials

Quartz sand was purchased from *Henan Hongda Filter Media Co., Ltd*, Henan Province. Potato residue was provided by *Yinguang Starch Factory*, Lintao County, Gansu Province. Waterborne polyurethane was produced by *Shenzhen Jitian Chemical Co., Ltd*. Petroleum ether, cyclohexane, sodium hydroxide, ethanol, methylene chloride, and trichloroethane were all produced by *Rionlon Bohua* (*Tianjin*) *Pharmaceutical & Chemical Co., Ltd*. Engine oil (10 W-40) was produced by the *Lubricating Oil Branch of China Petroleum Corporation*. Diesel was purchased from local petrol stations. Methylene blue was produced by *Tianjin Damao Chemical Reagent Factory*. Oil red O was purchased from *Shanghai Zhongqin Chemical Reagent Co., Ltd*. Deionized water was made in the laboratory. The relevant parameters of the several oils and water used for separation are shown in Table S1 (Supporting Information).

2.2. Fabrication of superhydrophilic and underwater superoleophobic quartz sand filter media (PR@QS)

Quartz sand was sieved with stainless steel, washed with distilled water, dried in an oven at 110 °C, washed twice with ethanol, and dried to obtain pretreated quartz sand. Twenty grams of potato residue was sieved with a 400-mesh stainless steel sieve, immersed in 500 mL of a 9% NaOH aqueous solution at room temperature, ultrasonically shaken with an ultrasonic oscillator (KQ5200DB, Kunshan Ultrasonic Instrument *Co., Ltd*, China) for 2 h, sealed and placed in a 0 °C environment for 12 h. After drying at 100 °C for 1 h, activated potato residue was obtained. Activated potato residue was added to 500 mL of ethanol and magnetically stirred at room temperature for 4 h. Then, 4 g of waterborne polyurethane was added and stirred for 15 min. Finally, the pretreated quartz sand was immersed in the prepared mixed solution, sealed, and immersed at room temperature for 48 h; dried at 80 °C; repeatedly washed with deionized water, and dried again at 80 °C. Superhydrophilic and underwater superoleophobic quartz sand filter media (hereafter referred to as PR@QS) were obtained.

2.3. Fabrication of superhydrophobic and superoleophilic quartz sand filter media (OTS-ZnO@QS)

Superhydrophobic and superoleophilic quartz sand filter media were prepared based on our previous research (Liu *et al.* 2018b). Briefly, 25 g tris(hydroxymethyl)aminomethane solid particles were dissolved in 500 mL of an ethanol solution, and then 1.7 g ZnO nanoparticles and 1.0 mg dopamine hydrochloride were added and stirred. Next, 40 g pretreatment quartz sand was added and ultrasonically dispersed at 40 kHz for 5 min using an ultrasonic oscillator and then stirred for 16 h at 650 rpm using a JB-2 thermostatic stirrer. The quartz sand filter was finally leached and dried in an oven at 80 °C to obtain ZnO nanoparticle-roughened quartz sand. ZnO nanoparticle-roughened quartz sand was added to 10 mL octadecyltrichlorosilane (OTS) dissolved in 100 mL of a toluene solution, stirred at 650 rpm for 2 h, leached, and dried again in an oven at 80 °C. Superhydrophobic and superoleophilic quartz sand filter media (hereafter referred to as OTS-ZnO@QS) were obtained.

2.4. Characterization of PR@QS

A contact angle meter (KRÜSS DSA100, Germany) was used to measure the static contact angle of the PR@QS surface at room temperature. PR@QS was placed into water, 5 μL oil was dropped on the surface of PR@QS, photos were taken after 15 s, and the contact angle was measured. All contact angles were tested at different positions at least three times. X-ray energy spectroscopy (SEM, Kevex, USA) was used to study the surface morphology of the filter media. A PHI-5702 X-ray photoelectron spectrometer (XPS) was used to analyze the surface elements of the filter media. An infrared spectrum analyzer (FTIR) was used to analyze the chemical structure of the filter media surface. Because the characterization of OTS-ZnO@QS has been studied in previous papers (Liu *et al.* 2018b), we do not repeat it here. Therefore, this paper only characterizes PR@QS.

2.5. Wetting stability of underwater superoleophobic PR@QS

PR@QS was immersed in an ethanol solution and placed in an ultrasonic oscillator. After ultrasonic oscillation for 12, 24, and 48 h at 40 kHz, PR@QS was removed and washed with deionized water five times. Then, PR@QS was dried, and the contact angle was measured to investigate the mechanical wear resistance of the filter media. Similarly, to study the acid and alkali resistance, PR@QS was immersed in aqueous solutions with pH values of 1, 5, 10, and 14 for 48 h. To study the surfactant resistance, PR@QS was immersed in a sodium dodecylbenzene sulfonate (SDBS) aqueous solution for 48 h. PR@QS was

exposed to air at room temperature, and the contact angles were measured after 30, 60, and 90 d to study the air exposure stability of the filter media.

2.6. Oil/water separator and separation method

The schematic diagram and a photograph of the oil/water separator are shown in Figure 1. The separator is mainly composed of two horizontally placed filtration columns with different lengths (10, 20, and 30 cm) and a 3-cm inner diameter, and a 30 cm-long and 3-cm inner diameter intake chamber. The two filtration columns are filled with OTS-ZnO@QS and PR@QS, respectively, and the packing porosity is calculated as 0.43. The inner side of the flange is padded with a 100-stainless mesh at both ends of the filtration column for fixing the filter media. The intake chamber is equipped with an inlet port. Water and oil are continuously injected from the inlet port at the same velocity by a peristaltic pump to form an oil/water mixture

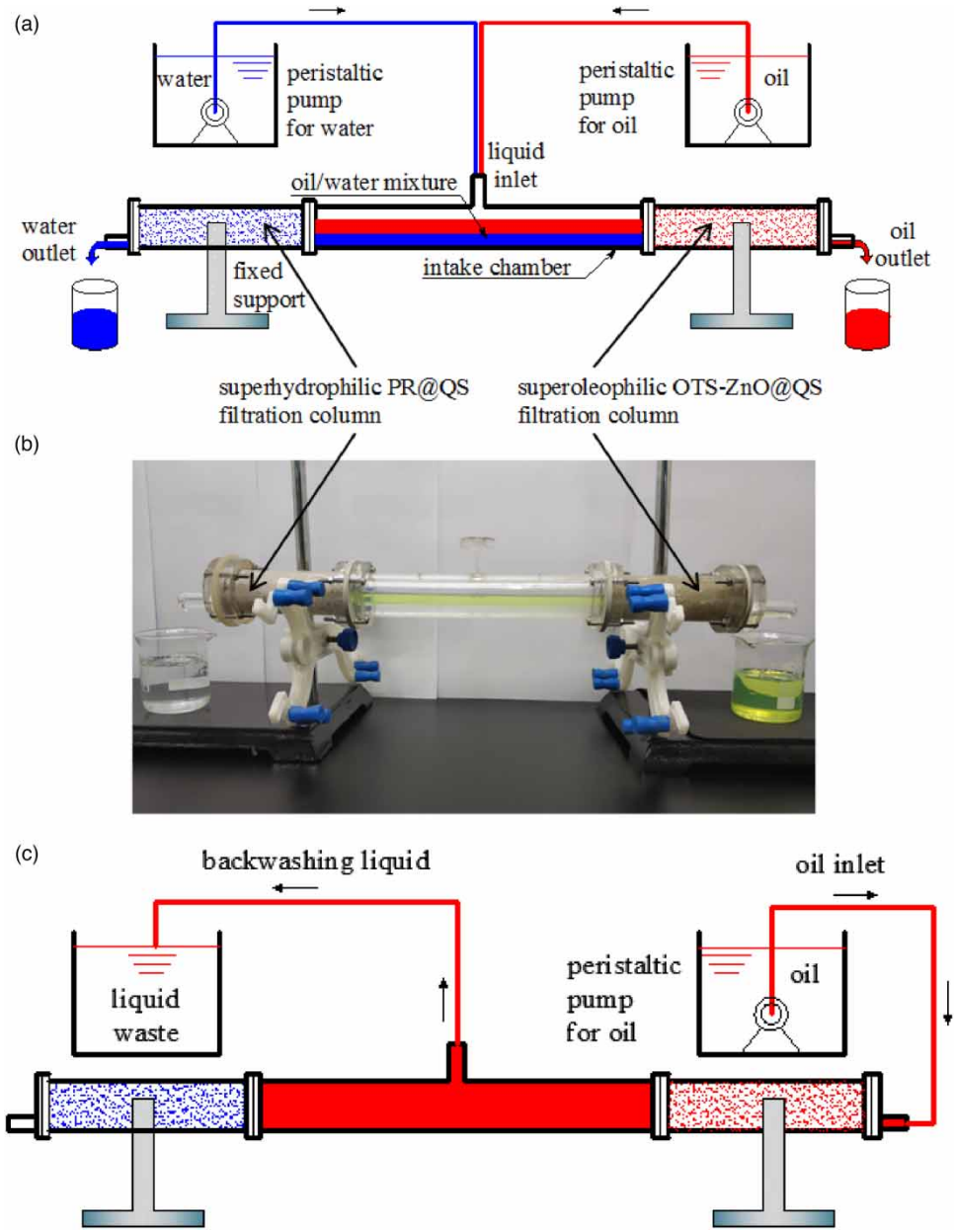

Figure 1 | (a) Schematic diagram and (b) photograph of the oil/water separator (oil was colored with oil red O, water was colored with methyl blue), and (c) schematic diagram of superoleophilic OTS-ZnO@QS column backwashing. Please refer to the online version of this paper to see this figure in colour: http://dx.doi.org/10.2166/wrd.2022.102.

(50%, V/V). The two filtration columns and the two ends of the intake chamber are connected with flanges. The filtration column packed with superhydrophilic PR@QS will allow water to pass and prevent oil from passing. Similarly, the filtration column packed with superoleophilic OTS-ZnO@QS will allow oil to pass and prevent water from passing. Thus, continuous separation of the oil/water mixture is realized. The oil content at the water outlet was determined by a total organic carbon/total nitrogen analyzer (MULTI N/C 2100, Analytikjena, Germany), and the water content at the oil outlet was measured by a fully automatic trace moisture tester (SN-WS200, *Qingdao Suntech Environmental Technology Company*, China). The separation efficiency of the mixed liquid is calculated according to Equation (1):

$$\eta = \frac{C_0 - C_e}{C_0} \times 100\% \tag{1}$$

where η is the oil (or water) separation efficiency, %; C_0 and C_e are the oil (or water) concentrations in the oil/water mixture and the water outlet (or oil outlet), respectively, mg/L.

Four different particle sizes of filter media (PR@QS and OTS-ZnO@QS) were packed into the filter column. The range of the particle diameters, equivalent particle diameters d_{eq}, and the capillary radius of packed filter layer R_c are shown in Table S2 (Supporting Information), where the equivalent particle sizes are represented by the geometric mean particle sizes.

2.7. Backwashing of the filtration column

During the separation process of the oil/water mixture, if the oil concentration in the water outlet sharply increased, it indicated that the oil phase had intruded the superhydrophilic PR@QS column. Similarly, if the water concentration in the oil outlet sharply increased, it indicated that the water phase had intruded the superoleophilic OTS-ZnO@QS column. When the filter column was intruded, it needed to be backwashed. For the OTS-ZnO@QS column, the operational process of backwashing is shown in Figure 1(c) as follows: oil is pumped from the oil outlet into the OTS-ZnO@QS column and flows into the intake chamber, and is then discharged from the intake chamber. For the PR@QS column, water is pumped. The amount of lyophilic liquid used in each backwashing was approximately five times the volume of the filter layer, that is, approximately 500 mL. The backwashing liquid could be re-separated.

3. RESULTS AND DISCUSSION

3.1. Characterization analysis

The potato residue is a by-product of cell fragments and residual starch particles produced in the production of potato starch. The main component is cellulose. The intramolecular hydrogen bonds and intermolecular hydrogen bonds of cellulose aggregate into different fibril structures with high crystallinity, which makes its highly reactive hydrogen bonds locked in the crystallization zone and difficult to contact with water. Therefore, intramolecular hydrogen bonds should be released by activation. The activated potato residue has more hydroxyl groups on its surface, which is easy to blend with waterborne polyurethane to form potato residue/waterborne polyurethane composite emulsion. When the quartz sand is immersed in the emulsion, the waterborne polyurethane adheres to the surface of the quartz sand, thus introducing potato residue into the quartz sand filter media surface.

As seen from the scanning electron microscope (SEM) images of PR@QS shown in Figure 2, the surface of pristine potato residue is smooth and complete without defects. After combined activation by alkali and ultrasonication, the surface of the potato residue becomes uneven, with the formation of more pores and cracks, indicating that the activation process is successful. The surface of pristine quartz sand has more edges and corners, and its surface porosity is not developed. While the surface of PR@QS is covered with a thin film and there are micro/nano scale pits, it should be a potato residue coating layer, which indicates that there is a rough structure when potato residue is introduced.

Potato residue is mainly composed of cellulose, hemicellulose, and lignin. The $-CH_2OH$ group of activated cellulose will form a condensation reaction with the –OH of quartz sand to graft the hydrophilic group onto the surface of quartz sand. It can be seen from the FTIR spectra (Figure 3(a)) that, for PR@QS, there is a strong stretching vibration peak of C–O belonging to alcohol, phenol, ether, or ester at 1,079 cm^{-1}. At 2,921 cm^{-1}, there is an aliphatic group –CH stretching vibration peak (Deng *et al.* 2011). These groups belong to the characteristic peak of potato residue (Zhang *et al.* 2015) and do not exist in the spectrogram of pristine quartz sand, indicating that potato residue has been coated to the surface of quartz sand. At

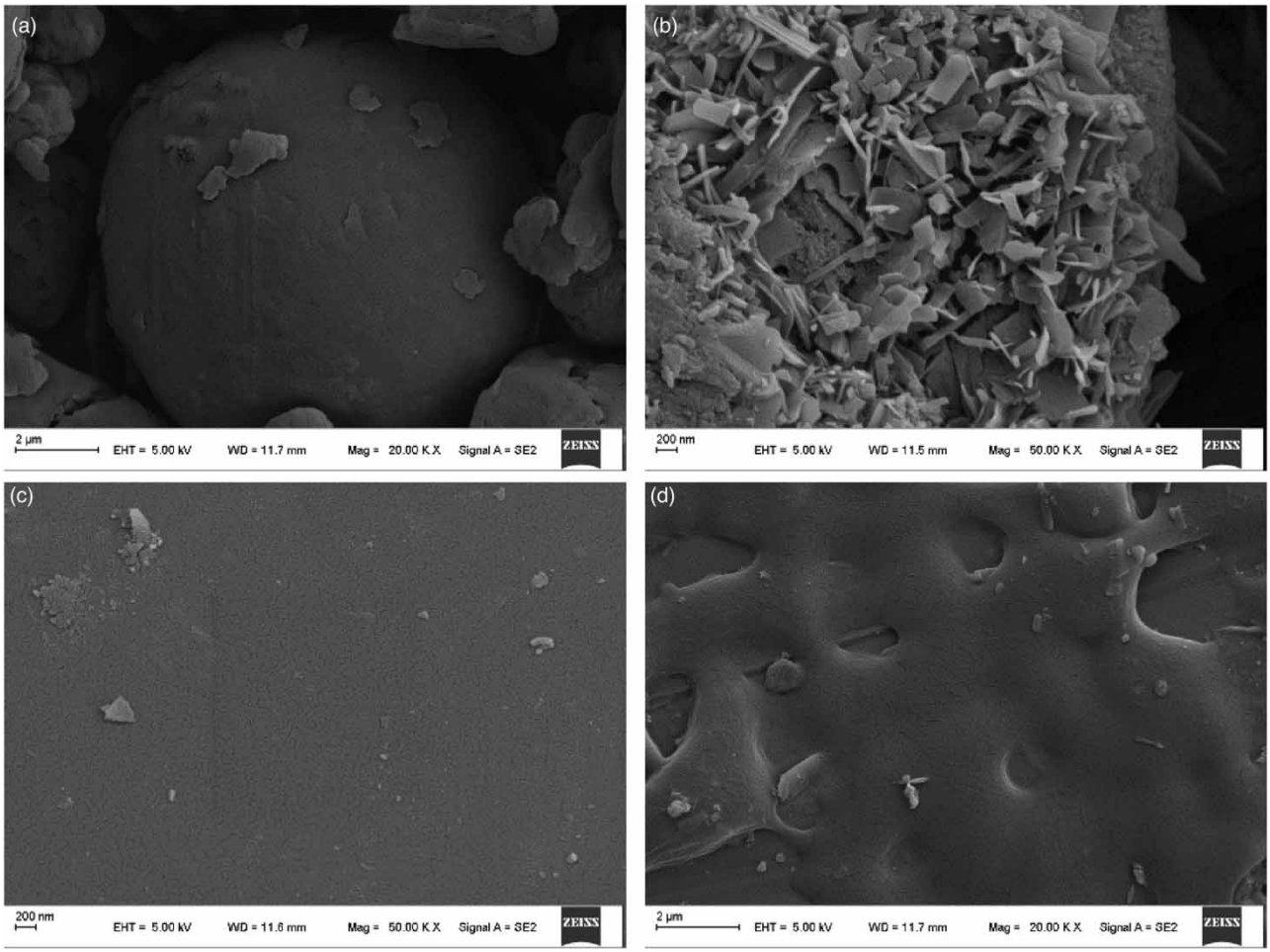

Figure 2 | SEM images of (a) pristine and (b) activated potato residue, and (c) pristine quartz sand and (d) PR@QS.

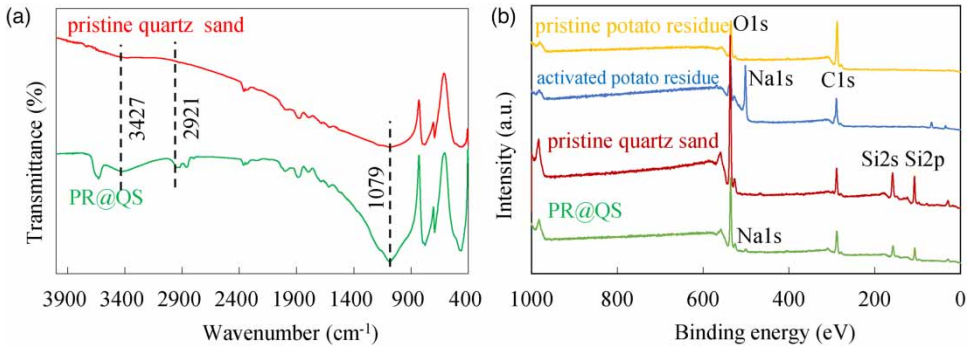

Figure 3 | (a) FTIR spectra of pristine quartz sand and PR@QS. (b) XPS spectra of pristine and activated potato residue, pristine quartz sand, and PR@QS.

3,427 cm^{-1}, the stretching vibration peak of O–H is wider and stronger (Fang *et al.* 2008), indicating that there are more hydroxyl groups on the surface of PR@QS than on pristine quartz sand.

The same results can be obtained from XPS analysis (as shown in Figure 3(b)). Before activation, potato residue was mainly composed of C (288.0 eV, 77.98%), O (535.6 eV, 19.70%), and N (411.6 eV, 1.32%), with a small amount of Si (103.5 eV, 0.99%). After activation, the Na (501.2 eV) element content reached 14.97%, which was induced by NaOH activation.

The concentration of O (31.30%) was higher than that before activation, which was generated by the introduction of –OH and cellulose molecules. Pristine quartz sand is mainly composed of O (532.8 eV) and Si (103.5 eV), with atomic concentrations of 69.55 and 30.45%, respectively. For PR@QS, Na (501.2 eV, 1.04%) and C (288.0 eV, 38.78%), the characteristic elements of activated potato were introduced, and the content of Si (103.5 eV, 15.23%) was reduced, indicating that the surface of PR@QS was coated with potato residue, thus reducing Si exposure.

3.2. Surface wettability

The wettability of a solid surface can be represented by the contact angle. According to our previous study, the water contact angle of OTS-ZnO@QS is 154.1°, while the oil contact angle is approximately 0°. OTS-ZnO@QS has superhydrophobic and superoleophilic characteristics (Liu *et al.* 2018b).

For PR@QS, both water and oil (dichloromethane) can rapidly spread on the PR@QS surface in air, and the contact angle is approximately 0°, as shown in Figure 4(a), indicating that PR@QS is superhydrophilic and superoleophilic in air. Placing PR@QS in water and then dropping oil onto its surface leads to the formation of spherical shaped oil, as shown in Figure 4(b), indicating that PR@QS has underwater superoleophobic characteristics. The underwater oil contact angles of all four light oils and two heavy oils are shown in Figure 4(c). Figure 4(c) shows that the underwater engine oil contact angle is the smallest at 151.6° ± 1.7°, while that of trichloromethane is the highest at 160.9° ± 1.7°.

The superhydrophilic and superoleophilic characteristics of the PR@QS surface are mainly attributed to hydroxyl groups, which have a strong affinity to water, and organic nonpolar functional groups, which have a strong affinity to the oil contained in the potato residue. At the same time, the rough structure of the potato residue on the PR@QS surface makes the water and oil attain the Wenzel state (Milne *et al.* 2011) in air, further increasing the lyophilicity of PR@QS. The Wenzel

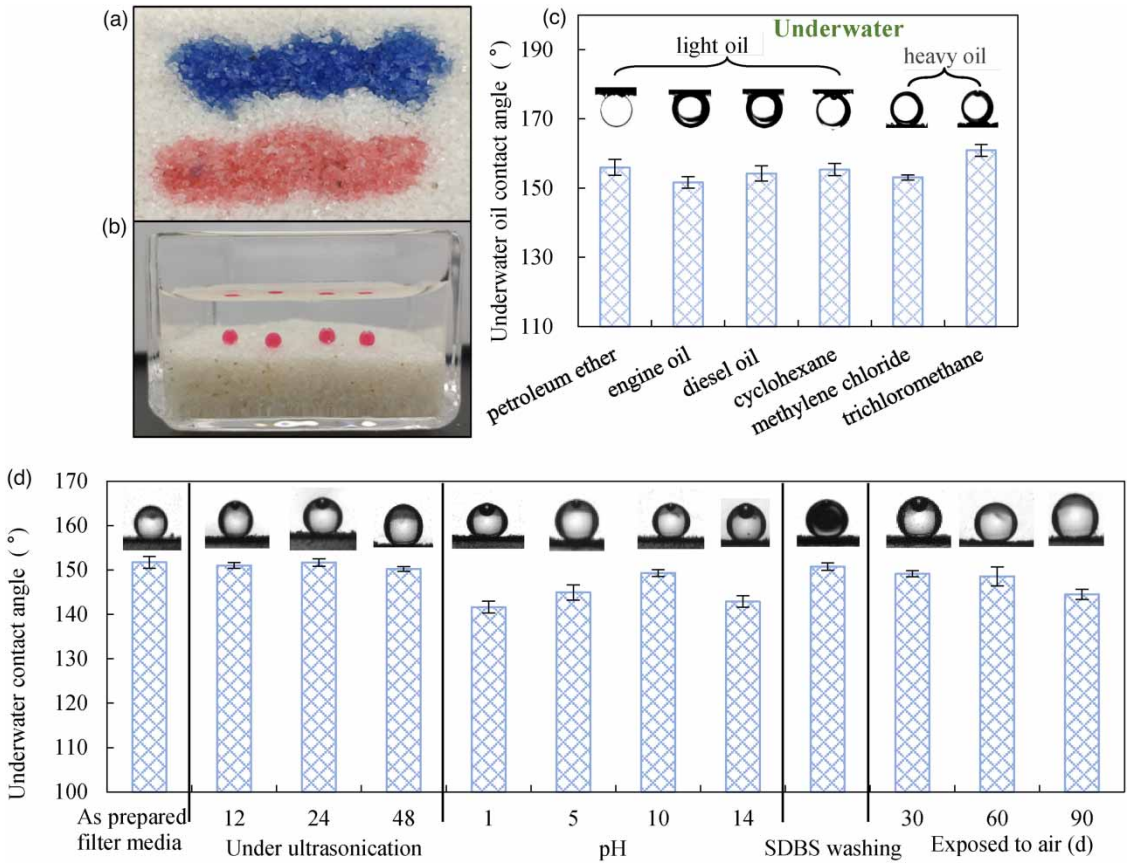

Figure 4 | Photograph of (a) water and oil dripped on the PR@QS surface in the air (water was dyed with methylene blue and oil was dyed with methylene chloride O), and (b) underwater oil dropped on the PR@QS surface. (c) Underwater oil contact angles of different oils for PR@QS. (d) Wetting stability of PR@QS. Please refer to the online version of this paper to see this figure in colour: http://dx.doi.org/10.2166/wrd.2022.102.

state is expressed as:

$$\cos\theta_W = r\cos\theta_O \tag{2}$$

where θ_W is the apparent oil contact angle in the air at the Wenzel state, °; θ_O is the intrinsic oil contact angle in the air, °; and r is the roughness of the PR@QS surface, which is defined as the ratio of the total area of the solid surface to the projected area.

When PR@QS is prewetted with water, the PR@QS surface is covered with a water film. At this time, when oil is dropped onto the PR@QS surface, the oil droplets on water film, so the oil–water–PR@QS three-phase Cassie state (Cassie 1948; Michielsen & Lee 2007) forms on the PR@QS surface, making the oil contact angle greater than 150°. Cassie relationships can be expressed as:

$$\cos\theta_{CB-O/W} = r_{SO}f_{SO}\cos\theta_O + (1 - f_{SO})\cos\theta_{OW} \tag{3}$$

where $\theta_{CB-O/W}$ is the apparent underwater oil contact angle in the Cassie relation, °; f_{SO} is the ratio of the projected area of the contact part between the solid and the oil and the total projected area of the solid. Since the contact line between the oil phase and water is considered a horizontal line, $1 - f_{SO}$ is the ratio of the oil/water contact surface to the total projected area of the solid. r_{SO} is the 'roughness' of the oil–solid contact area; θ_{OW} is the oil contact angle on the water film, which is 180°. It can be seen from Equation (3) that the water film increases the oil contact angle so that the oil droplets form a ball underwater, as shown in Figure 3(b).

Assuming that r_{SO} is the same as the roughness r of the PR@QS surface, then $r_{SO}\cos\theta_O$ is the apparent oil contact angle of the Wenzel state (Milne *et al.* 2011) in air on the PR@QS surface, which is equal to 0°. Substitute the values of θ_{OW} and $r_{SO}\cos\theta_O$ into Equation (3) to obtain:

$$\cos\theta_{CB-O/W} = 2f_{SO} - 1 \tag{4}$$

For example, the underwater contact angle of cyclohexane is 155.4°. Substituting it into Equation (4), it can be calculated that $f_{SO} = 4.5\%$, that is, 95.5% of the filter surface is covered by water film.

3.3. Wetting stability of PR@QS

The wetting stability of PR@QS was also studied, as shown in Figure 4(d). Ultrasound oscillation is often used to clean impurities on the surfaces of substances because the ultrasonic process can physically damage these impurities. Therefore, oscillation is often used to study the mechanical stability of superwettable surfaces (Milionis *et al.* 2016). Figure 4(d) shows that the underwater oil contact angle remains at 150.2° ± 0.5° after 48 h of oscillation, indicating that PR@QS has strong mechanical stability. Under acidic and alkaline conditions, the underwater superoleophobicity of PR@QS slightly decreases. The underwater oil contact angles were 141.6° ± 1.3° and 144.9° ± 1.7° at pH 1 and pH 5, respectively, and 149.3° ± 0.7° and 142.9° ± 1.3° at pH 10 and pH 14, respectively. These findings indicate that PR@QS does not have strong acid resistance but has good alkali resistance. After washing with SDBS, the underwater oil contact angle of PR@QS decreased to 150.8° ± 0.9°, still maintaining a good underwater superoleophobic property. This finding indicates that PR@QS has strong resistance to surfactants. After a long exposure to air, the underwater oil contact angle of PR@QS decreased to some extent, but the decrease was not significant. After 90 d, the underwater oil contact angle was 144.5° ± 1.11°, which still had good underwater oleophobicity. Therefore, PR@QS could be stored for a long time.

3.4. Separation performance of oil/water mixtures

3.4.1. Separation efficiency of different oil/water mixtures

When the particle sizes of the two-filter media are 0.355–0.577 mm and the length of the filter columns are 10 cm, the separation efficiencies of the five oil/water mixtures are shown in Figure 5. As seen from Figure 5(a) and (b), water is invisible to the naked eye in the oil outlet beaker and the oil cannot be observed with the naked eye at the water outlet beaker. After separating the 1 L mixture, the oil content at the water outlet and the water content at the oil outlet were determined. The oil and water separation efficiencies of all five kinds of oils were between 99.40 and 99.99%. These high separation efficiencies can be explained by the capillary pressure of the liquid in the filter layer, as shown in Figure 6 (Bigui *et al.* 2019). As seen

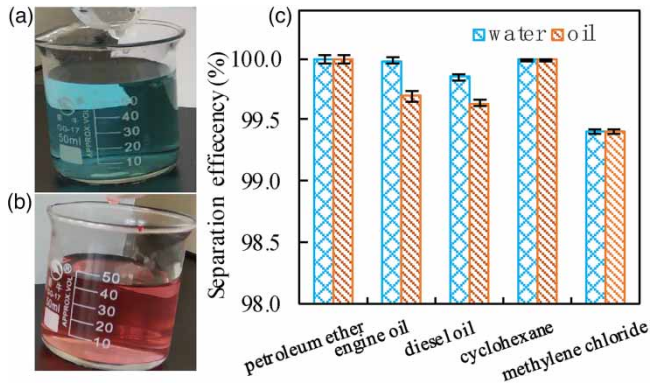

Figure 5 | Photograph of (a) water outlet and (b) oil outlet, and (c) separation efficiencies of 0.355–0.577 mm filter media for the five oil/water mixtures.

from Figure 6, for superhydrophobic and superoleophilic OTS-ZnO@QS, the capillary pressure of the oil points to the outlet side of the filter layer, driving the oil phase flow through the filter layer, while the capillary pressure of the water points to the inlet side, preventing the water phase from passing through the filter layer (Liu *et al.* 2018b). Therefore, the outlet of the OTS-ZnO@QS filter column is oil. Similarly, for superhydrophilic and underwater superoleophobic PR@QS, the capillary pressure drives the water phase flow through the filter layer and prevents the oil phase from passing through (Yong *et al.* 2016), so the outlet is water.

3.4.2. Intrusion pressure

According to the Laplace equation (Ge *et al.* 2017), the capillary force in the filter layer is:

$$\Delta P_{\mathrm{cal}} = \frac{2\gamma\cos\theta}{R_{\mathrm{c}}} \tag{5}$$

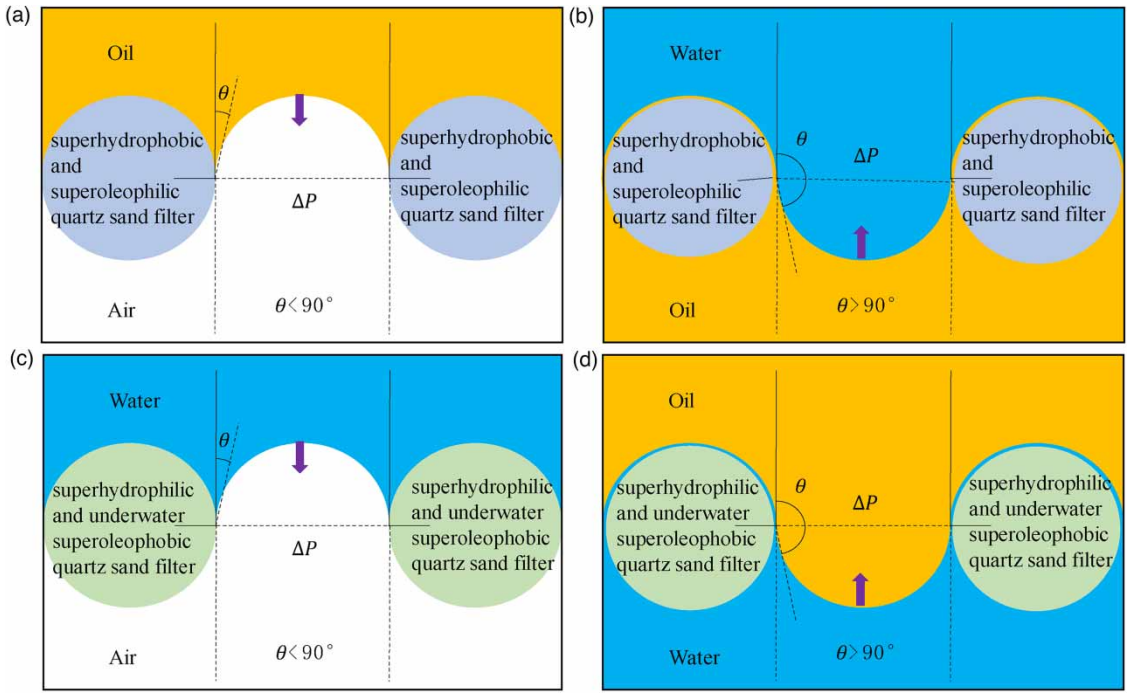

Figure 6 | Capillary pressure of (a) oil in air and (b) underoil water in superhydrophobic and superoleophilic filter media; capillary pressure of (c) water in air and (d) underwater oil in superhydrophilic and underwater superoleophobic filter media (Bigui *et al.* 2019).

where ΔP_{cal} is the theoretical capillary pressure, Pa; R_c is the radius of the capillary in the filter layer, m, which is listed in Table S2 (Supporting Information); γ is the surface tension of the lyophobic liquid, N/m; and θ is the underoil water contact for the OTS-ZnO@QS or the underwater oil contact for the PR@QS.

During the separation process, due to the height of the liquid level in the intake chamber, hydrostatic pressure will be generated on the filter layer. Theoretically, when the hydrostatic pressure is less than the theoretical capillary pressure, the lyophobic liquid will not intrude on the filter layer; when the hydrostatic pressure exceeds the theoretical capillary pressure, the lyophobic liquid will intrude the filter layer (Li *et al.* 2018a). When the filter layer is just intruded, the hydrostatic pressure is called the theoretical intrusion pressure, which is equal to the capillary force ΔP_{cal} (Li *et al.* 2018a).

To verify the theoretical intrusion pressure of the filter media, a single lyophobic liquid was used for the test, as shown in Figure 7(a). In this test, a glass tube with a 1-cm inner diameter was filled to a height of 5 cm with filter media, the filter layer was prewet with lyophilic liquid, and then the lyophobic liquid was slowly poured over the glass tube. When the height of the lyophobic liquid is small, the liquid is intercepted on the surface of the filter layer due to capillary pressure. When lyophobic liquid just begins to intrude, the hydrostatic pressure on the filter layer is the experimental intrusion pressure, and its expression is (Li *et al.* 2018b):

$$\Delta P_{exp} = \rho g h_{max} \tag{6}$$

where ΔP_{exp} is the experimental intrusion pressure, Pa; ρ is the density of the lyophobic liquid, kg/m^3; g is the gravitational acceleration, 9.81 m/s^2; and h_{max} is the height of the lyophobic liquid when it just begins to intrude, m.

The theoretical and experimental values of the intrusion pressure of several lyophobic liquids on the two filter layers are slightly different, as shown in Figure 7(b). As seen from Equation (5) and Figure 7(b), the theoretical intrusion pressure is related to the surface tension and contact angle of the lyophobic liquid. Since the surface tension of water is the maximum, it has the maximum intrusion pressure. The experimental and theoretical values are up to 0.29 $\pm$ 0.01 and 0.31 kPa, respectively. The theoretical intrusion pressure of engine oil is the lowest, 0.14 kPa, but the experimental intrusion pressure is as high as 0.27 $\pm$ 0.02 kPa. The reason for this difference is that the viscosity of engine oil is too high and the flow speed is too slow, so the experimental error is relatively large.

3.4.3. Hydraulic conductivity

The hydraulic conductivity of the filter layer is another important evaluation index of the oil/water separation performance, which will determine the rate of oil/water separation. The hydraulic conductivity of the filter layer can be described by Darcy's law (Firdaouss *et al.* 1997):

$$Q = \frac{F\Delta h}{L} \tag{7}$$

where Q is the flow of lyophilic liquid, m^3/h; is the hydraulic conductivity, m/h; F is the cross-sectional area, m^2; L is the length of the filter layer, m; and Δh is the head loss of the filter layer, m. During the oil/water separation process, the

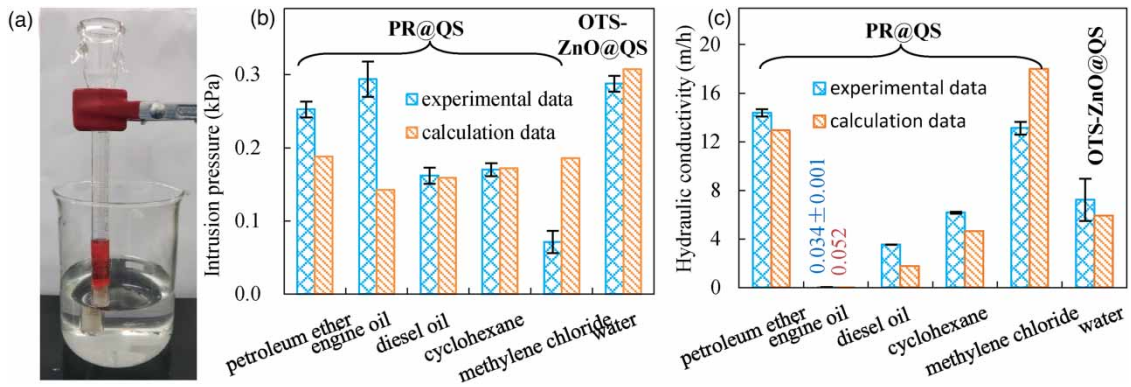

Figure 7 | Theoretical and experimental values of the (a) intrusion pressure of several lyophobic liquids and (b) the hydraulic conductivity of several lyophilic liquids on the two filter media.

intake chamber is photographed, the depths of oil and water in the chamber are measured, and the experimental hydraulic conductivity of the filter layer can be calculated according to Darcy's law. See Section S3 for details (Supporting Information). The experimental hydraulic conductivity is shown in Figure 7(c).

The flow of liquid through the filter layer can be expressed by the Kozeny–Carman (KC) equation, which was proposed by Kozeny (1927) and improved by Carman (1937). The KC equation can be further modified as (Taylor 1948):

$$K = \frac{1}{36C}\frac{\rho g}{\mu}\frac{\varepsilon^3}{(1-\varepsilon)^2}(\alpha d_{\mathrm{eq}})^2 \tag{8}$$

where C is the KC constant (≈5) (Kobayashi *et al.* 2017); ρ is the liquid density, kg/m^3; μ is the fluid viscosity, Pa·s; ε is the porosity of the filter layer, which is 0.43 for quartz sand; α is the shape factor of the filter particles, which is 0.78 for quartz sand; and d_{eq} is the equivalent diameter of the filter particle, m, as shown in Table S2 (Supporting Information). The theoretical hydraulic conductivity, which is calculated based on Equation (8), is also summarized in Figure 7(c).

Figure 7(c) shows that the experimental hydraulic conductivities of the six liquids in the filter layer are slightly different from those of the theoretical data, but the trends are consistent. As seen from Equation (8), the properties of the liquid (such as density and viscosity) have effects on the hydraulic conductivity. For the 0.355–0.577 mm particle size filter media layer, the experimental hydraulic conductivity of water in the PR@QS layer was up to 7.2 ± 1.7 m/h, slightly higher than the calculated value of 5.9 m/h. For OTS-ZnO@QS, the hydraulic conductivity of petroleum ether is the largest, 14.4 ± 0.3 m/h, due to the minimum viscosity. The value of methylene chloride is 13.13 m/h, followed by cyclohexane at 6.18 m/h and diesel at 3.56 m/h. Because the engine oil viscosity is too large, approximately 350 times that of petroleum ether, the hydraulic conductivity is very small, only 0.034 ± 0.001 m/h.

3.4.4. Effect of filter particle size on separation performance

To study the influence of filter particle size on the separation performance, four filter particle sizes were selected to separate the diesel/water mixture, and the distribution of the four particle sizes and their equivalent particle sizes are shown in Table S2. The results for a filter column with a length of 10 cm are shown in Figure 8(a)–(c). The separation efficiencies, separation volume before the first backwashing, and intrusion pressures decrease with the increase of particle size, while hydraulic conductivities increase with the increase of particle size. When the equivalent particle size is 0.99 mm, the separation efficiencies of water and oil decrease to 90%. The reduction in separation efficiency can be explained by the change in intrusion pressure. Substituting Equations (S2-4) and (S2-5) (Supporting Information) into Equation (5), the intrusion pressure can be expressed as:

$$\Delta P_{\mathrm{cal}} = \frac{6\alpha(1-\varepsilon)\gamma\cos\theta}{\varepsilon d_{\mathrm{eq}}} \tag{9}$$

where ε is the porosity of the filter layer and α is the shape factor of the filter media. It can be seen from Equation (9) that the intrusion pressure is inversely proportional to the equivalent particle size. When the particle size increases, the intrusion pressure rapidly decreases and the filter column is more likely to be intruded by lyophobic liquid (Li *et al.* 2020). Consequently, both the separation efficiency and separation volume before the first intrusion are decreased.

The theoretical and experimental intrusion pressures of filter media with different particle sizes are shown in Figure 8(b). For the OTS-ZnO@QS layer, the experimental intrusion pressure of water is slightly less than the calculated value. For the PR@QS layer, the oil intrusion pressure of the experimental value is consistent with the theoretical value when the equivalent diameter is greater than 0.4 mm, while the experimental value is far greater than the theoretical value when the equivalent diameter is less than 0.4 mm, but the trends are identical. From Equation (8), the hydraulic conductivities of the filter layer are proportional to the square of the particle size. The experimental and theoretical hydraulic conductivities of the filter layer with different particle sizes are shown in Figure 8(c). The experimental values are consistent with the theoretical values.

Through comprehensive analysis of the influences of particle size on separation efficiency, intrusion pressure, and hydraulic conductivity, it can be seen that if the filter media particle size is too large, it is not conducive to practical application for oil/water separation. Therefore, it is recommended that the equivalent particle size should not be greater than 0.6 mm.

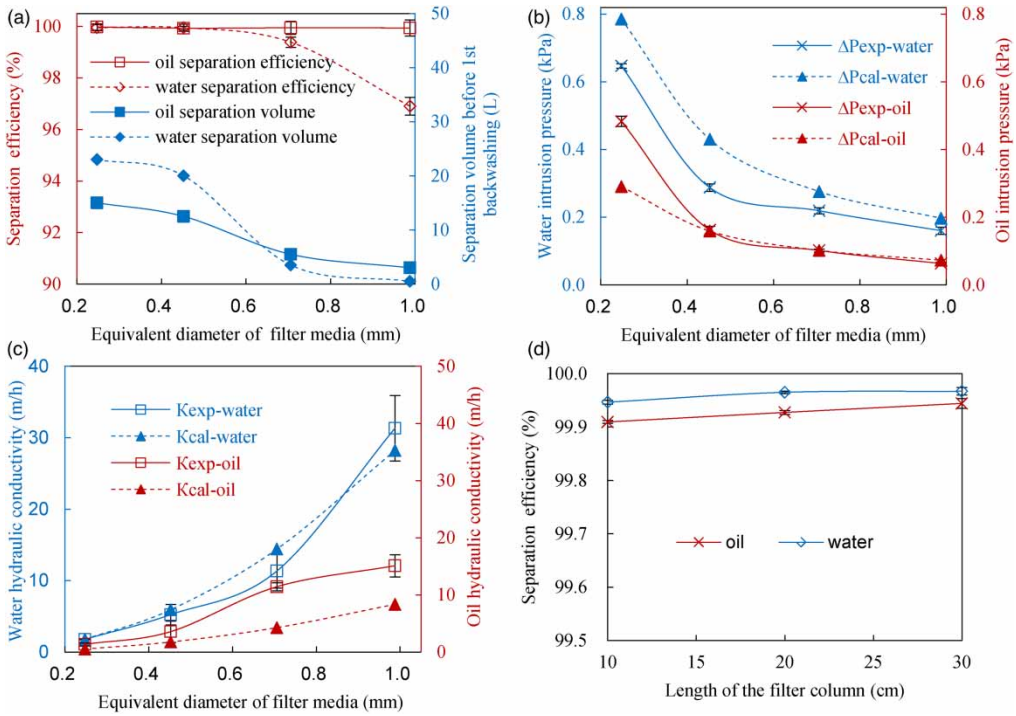

Figure 8 | (a) Separation efficiency, (b) intrusion pressure, and (c) hydraulic conductivity of the four filter particle sizes; (d) separation efficiency of different filter column lengths when the particle size is 0.355–0.577 mm.

3.4.5. Effect of the filter column length on separation performance

When the filter media particle size is 0.355–0.577 mm, the diesel/water mixture separation efficiencies of the three filter column lengths are shown in Figure 8(d). The separation efficiencies slightly increase with increasing filter column length. When the length of the filter column is 10 cm, the separation efficiencies are still as high as 99.91% for oil and 99.95% for water. Although the filtration column has a certain length, it is still dominated by the capillary action of the most forward filter layer. Similar to the mechanism of surface filtration (Leung & Choy 2018), the lyophobic liquid will not enter the filter layer, so the length of the filter layer has little influence on the separation efficiency (Zhou *et al.* 2019). Theoretically, the length of the filter column does not effect the intrusion pressure. Combining Equations (7) and (8), we can obtain:

$$\Delta h = 180\frac{\mu}{\rho g}\frac{(1-\varepsilon)^2}{\varepsilon^3}\frac{1}{(\alpha d_{eq})^2}\frac{Q}{F}L \tag{10}$$

Equation (10) is the calculation formula for the water head loss of the clean filter bed. Equation (10) shows that the head loss Δh is inversely proportional to the length of the filter column L. With the same flow rate, the head loss increases proportionally as the filter length increases. With the same head loss, the flow rate decreases with increasing filter length. Therefore, the length of the filter column should not be too long. In the actual separation, the filter layer length is recommended to be 10 cm.

3.4.6. Separation of the light oil/water mixture

To research the continuous separation performance of the light oil/water mixture, 0.355–0.577 mm filter media and 10 cm-long filtration columns were used to conduct continuous separation of the diesel and water mixture. The experimental results are shown in Figure 9 and Figure 10. Figure 9 shows that the oil and water separation efficiencies are greater than 99%. Once the filter layer is intruded by a lyophobic liquid, the oil concentration in the water effluent (or the water concentration in the oil effluent) sharply increases, and the oil (or water) droplets can be seen by the naked eye (as shown in the inset figures in Figure 9). At this time, the filter column should be backwashed. The PR@QS column was intruded by diesel when separating

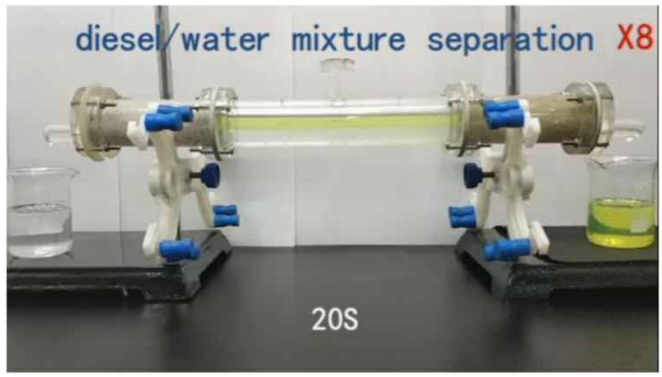

Figure 9 | Diesel/water mixture separation continuously.

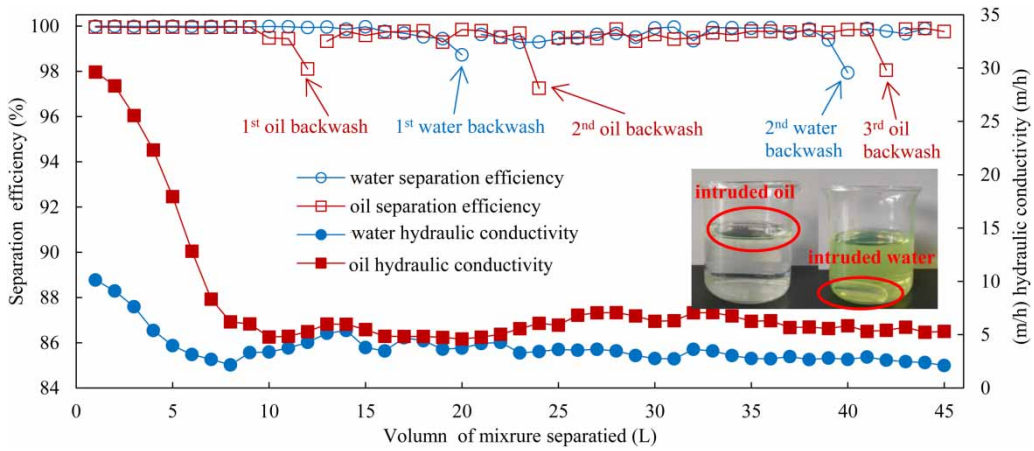

Figure 10 | Separation performance of the diesel/water mixture.

20 and 40 L mixtures. After backwashing, the separation efficiency is more than 99.5%. This is because when the lyophilic liquid reverse flows through the filter column, it should extrude the lyophobic liquid that has intruded into the filter column. The OTS-ZnO@QS column was intruded by water at the 12th, 24th, and 42nd L of separation, and the oil separation efficiency remained above 99.4%. It can also be seen from Figure 9 that after multiple intrusion/backwashing cycles, the separation efficiency remained unchanged, indicating that the filter column has good recovery performance and can continuously separate light oil/water in large quantities.

As the separation continues, the hydraulic conductivity of the filter column gradually decreases. The hydraulic conductivity of water gradually decreases from 10.1 m/h at the beginning to 4.0 m/h at the 5th L mixture separated and then fluctuates between 2.1 and 6.1 m/h. For diesel, the initial hydraulic conductivity is up to 29.6 m/h, gradually falls to 6.2 m/h at the 8th L mixture separated, and then fluctuates between 4.8 and 7.1 m/h. The initial stage in which the hydraulic conductivity decreases can be called the 'ripening stage'. When the lyophilic fluid flows through the filter layer, it produces a shear force on the filter layer, thus making the metastable filter media move, making the filter layer denser and the pores smaller. When the filter layer is ripening, the head loss tends to be stable.

3.4.7. Separation of the heavy oil/water mixture

In the same way, 0.355–0.577 mm filter media and 10 cm-long filtration columns are used to conduct continuous separation of the dichloromethane and water mixture. The experimental results are shown in Figure 11. From Figure 11, it can be seen that the separation efficiencies of oil and water are all greater than 99.6%. The PR@QS column is intruded by dichloromethane when separating the 5 and 23 L mixtures, and the OTS-ZnO@QS column is intruded by water only once, at the 7th L of separation. Compared with diesel, dichloromethane and water are less intruded when separated, which may be

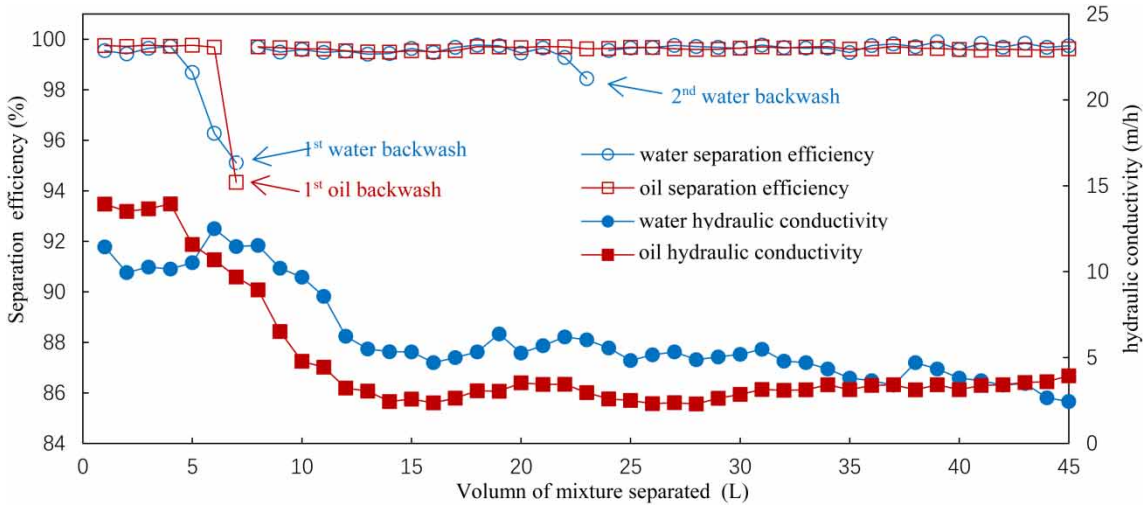

Figure 11 | Separation performance of the dichloromethane/water mixture.

Table 1 | Separation performance studied by prior researchers

Coating material	Substrates	Wettability	Type of liquid	Separated volume per cycle (mL)	Number of circles	Total separated volume (L)	η after circulation	Ref.
Graphene	Stainless steel mesh	Superhydrophobic	Kerosene	80	20	1.6	95%	Tang *et al.* (2019)
Thiolated castor oil	Stainless steel mesh	Superhydrophobic	Absolute ethanol	15	25	0.375	98.8%	Shang *et al.* (2019)
NiS nanorod	Ni mesh	Superhydrophobic	Kerosene	/①	20	/	95%	Yin *et al.* (2020b)
COF	Stainless steel mesh	Superhydrophobic	Petroleum ether	50	50	2.5	99.5%	Jiang *et al.* (2019)
TiO_2 and perfluorodecyltriethoxysilane (PFDTS)	Copper mesh	Superhydrophobic	Benzene	20	100	2.0	98%	Tudu & Kumar (2019)
Waterborne composite	Stainless steel mesh	Underwater superoleophobic	Kerosene	/	30	/	95%	Tian *et al.* (2019)
PA-Sn@MH and TiO_2	Stainless steel mesh	Underwater superoleophobic	Dodecane	20	210	4.2	98.5%	Meng *et al.* (2020)
Copper and dodecanethiol	Stainless steel mesh	Superhydrophobic	Kerosene	/	50	/	98.9%	Li *et al.* (2018c)
Copper	Stainless steel mesh	Underwater superoleophobic	Kerosene	/	50	/	99.2%	Li *et al.* (2018c)
OTS and ZnO	Quartz sand particle	Superhydrophobic	Diesel oil Methylene chloride	Continuous		45 45	99.4% 99.5%	This paper
Potato residue	Quartz sand particle	Underwater superoleophobic	Diesel oil Methylene chloride	Continuous		45 45	99.5% 99.6%	This paper

Note: ①/means not mentioned.

caused by two reasons. The first reason is that the theoretical intrusion pressure of dichloromethane is 1.3 times that of diesel, so the PR@QS column is more likely to be intruded by diesel than by dichloromethane. Second, diesel oil is a mixture separated light oil, it is in the upper layer in the intake chamber, and water is in the lower layer. As a result, the hydrostatic pressure of water is higher than that of the dichloromethane/water mixture, so water more easily intrudes on the OTS-ZnO@QS column.

Similar to the process of separating the diesel/water mixture, the hydraulic conductivity of water gradually decreases from 10.3 m/h at the beginning to 5.5 m/h at the 13th L of the mixture separated and then fluctuates between 2.0 and 6.2 m/h. For dichloromethane, the hydraulic conductivity decreases from 13.5 to 3.0 m/h at 13th L of the mixture separated and then fluctuates between 2.4 and 3.9 m/h. The 'ripening stage' is before filtering the 8th L of the mixture is separated. The experimental results show that the separator can separate heavy oil and water mixtures continuously and efficiently in large quantities.

Some researchers have also studied the repeated separation of oil/water mixtures with special wettability materials, and the relevant research results are listed in Table 1. Compared with previous research results, this paper still has greater separation efficiency under the condition of a larger separation volume.

4. CONCLUSIONS

In summary, we report a method for continuous oil/water separation using special wettability materials. Two separation columns were filled with two kinds of superwettable granular filters with opposite wettabilities, and the two separation columns were connected with the same separation chamber. The superhydrophobic and superoleophilic filter column only allows the oil phase to pass through, not the water phase. The superhydrophilic and underwater superoleophobic filter column only allows the water phase to pass through, not the oil phase. Consequently, both the oil phase and water phase of the oil/water mixture in the separation chamber can flow out from its own filter column, which realizes the separation of oil and water continuously. Superhydrophobic and superoleophilic filter media were prepared according to previous research results by our team, and superhydrophilic and underwater superoleophobic filter media were prepared by activated potato residue coated with quartz sand. The experimental results show that all the separation efficiencies of the five oil/water mixtures (petroleum ether, engine oil, diesel oil, cyclohexane, methylene chloride, and trichloromethane) were greater than 99.4%. It is recommended that the equivalent diameter of the granular filter should not be greater than 0.6 mm and the length of the filter layer should be 10 cm. In the continuous separation of oil/water mixtures, the backwashing method can be used to extrude the lyophobic liquid that intrudes the filter layer and to recover the separation efficiency of the filter layer. Therefore, the oil/water separator can separate oil/water mixtures continuously and efficiently and can be applied to practical industrial production.

FUNDING

This work was supported by the National Natural Science Foundation of China (Nos 51668032 and 52060014) and the Foundation of A Hundred Youth Talents Training Program of Lanzhou Jiaotong University (No. 152022).

DATA AVAILABILITY STATEMENT

All relevant data are included in the paper or its Supplementary Information.

REFERENCES

Bigui, W., Cheng, Y., Jianlin, L., Gang, W., Liang, D., Xiaosan, S., Fuping, W., Hua, L. & Qing, C. 2019 Fabrication of superhydrophilic and underwater superoleophobic quartz sand filter for oil/water separation. *Separation and Purification Technology* **229**, 115808.

Budnyak, T. M., Pylypchuk, I. V., Tertykh, V. A., Yanovska, E. S. & Kolodynska, D. 2015 Synthesis and adsorption properties of chitosan-silica nanocomposite prepared by sol-gel method. *Nanoscale Research Letters* **10**, 87.

Calvo, L. S., Leclerc, J. P., Tanguy, G., Cames, M. C., Paternotte, G., Valentin, G., Rostan, A. & Lapicque, F. 2010 An electrocoagulation unit for the purification of soluble oil wastes of high COD. *Environmental Progress & Sustainable Energy* **22**, 57–65.

Carman, P. C. 1937 Fluid flow through granular beds. *Transactions of the Institution of Chemical Engineers* **15**, 150–156.

Cassie, A. B. D. 1948 Contact angles. *Discussions of the Faraday Society* **3**, 11–16.

Cheng, Y. Y., Lu, S. X., Xu, W. G. & Tao, H. 2017 Fabrication of Cu-CuO-Fe_2O_3/Fe anti-sticky and superhydrophobic surfaces on an iron substrate with mechanical abrasion resistance and corrosion resistance. *New Journal of Chemistry* **41**, 5205–5214.

Cheng, Q.-Y., Zhao, X.-L., Li, Y.-D., Weng, Y.-X. & Zeng, J.-B. 2019 Robust and nanoparticle-free superhydrophobic cotton fabric fabricated from all biological resources for oil/water separation. *International Journal of Biological Macromolecules* **140**, 1175–1182.

Deng, H., Lu, J. J., Li, G. X., Zhang, G. L. & Wang, X. G. 2011 Adsorption of methylene blue on adsorbent materials produced from cotton stalk. *Chemical Engineering Journal* **172**, 326–334.

Du, C., Wang, J., Chen, Z. & Chen, D. 2014 Durable superhydrophobic and superoleophilic filter paper for oil–water separation prepared by a colloidal deposition method. *Applied Surface Science* **313**, 304–310.

Du, X., Wang, Q. & Wang, X. 2019 Underwater superoleophobic mesh with transformable micro-nano structure for ultrafast oil/water separation. *Surface and Coatings Technology* **358**, 806–816.

Fang, X.-Y., Wang, T.-J., Wu, H.-X. & Jin, Y. 2008 Surface chemical modification of nanosized oxide particles with a titanate coupling reagent in isopropanol. *Industrial & Engineering Chemistry Research* **47**, 1513–1517.

Firdaouss, M., Guermond, J.-L. & Le Quéré, P. 1997 Nonlinear corrections to Darcy's law at low Reynolds numbers. *Journal of Fluid Mechanics* **343**, 331–350.

Ge, B., Zhang, Z., Zhu, X., Men, X. & Zhou, X. 2014 A superhydrophobic/superoleophilic sponge for the selective absorption oil pollutants from water. *Colloids and Surfaces A: Physicochemical and Engineering Aspects* **457**, 397–401.

Ge, B., Zhu, X., Li, Y., Men, X., Li, P. & Zhang, Z. 2015 Versatile fabrication of magnetic superhydrophobic foams and application for oil–water separation. *Colloids and Surfaces A: Physicochemical and Engineering Aspects* **482**, 687–692.

Ge, J., Zhang, J., Wang, F., Li, Z., Yu, J. & Ding, B. 2017 Superhydrophilic and underwater superoleophobic nanofibrous membrane with hierarchical structured skin for effective oil-in-water emulsion separation. *Journal of Materials Chemistry A* **5**, 497–502.

Hafiz, A. A., El-Din, H. M. & Badawi, A. M. 2005 Chemical destabilization of oil-in-water emulsion by novel polymerized diethanolamines. *Journal of Colloid and Interface Science* **284**, 167–175.

Huang, Y., Li, H., Wang, L., Qiao, Y., Tang, C., Jung, C., Yoon, Y., Li, S. & Yu, M. 2015 Ultrafiltration membranes with structure-optimized graphene-oxide coatings for antifouling oil/water separation. *Advanced Materials Interfaces* **2**, 1400433.

Jamalludin, M. R., Hubadillah, S. K., Harun, Z., Othman, M. H. D. & Yunos, M. Z. 2019 Novel superhydrophobic and superoleophilic sugarcane green ceramic hollow fibre membrane as hybrid oil sorbent-separator of real oil and water mixture. *Materials Letters* **240**, 136–139.

Jiang, Y., Liu, C., Li, Y. & Huang, A. 2019 Stainless-steel-net-supported superhydrophobic COF coating for oil/water separation. *Journal of Membrane Science* **587**, 117177.

Jing, Z., Ding, J., Zhang, T., Yang, D., Qiu, F., Chen, Q. & Xu, J. 2019 Flexible, versatility and superhydrophobic biomass carbon aerogels derived from corn bracts for efficient oil/water separation. *Food and Bioproducts Processing* **115**, 134–142.

Kintisch, E. 2010 Gulf oil spill, an audacious decision in crisis gets cautious praise. *Science* **329**, 735–736.

Kobayashi, I., Owada, H., Ishii, T. & Iizuka, A. 2017 Evaluation of specific surface area of bentonite-engineered barriers for Kozeny-Carman law. *Soils and Foundations* **57**, 683–697.

Kozeny, J. 1927 Uber kapillare Leitung des Wassers im Boden. *Sitzungsber Akad Wiss Wien* **136**, 271–306.

Leung, W. W.-F. & Choy, H.-F. 2018 Transition from depth-to-surface filtration for a high-efficiency, high-skin effect, nanofiber filter under continuous nano-aerosol loading. *Chemical Engineering Science* **182**, 67–76.

Li, K., Zeng, X., Li, H., Lai, X. & Xie, H. 2014 Facile fabrication of superhydrophobic filtration fabric with honeycomb structures for the separation of water and oil. *Materials Letters* **120**, 255–258.

Li, J., Guan, P., Zhang, Y., Xiang, B., Tang, X. & She, H. 2017 A diatomite coated mesh with switchable wettability for on-demand oil/water separation and organic pollutants adsorption. *Separation and Purification Technology* **174**, 275–281.

Li, H., Liang, T., Lai, X., Su, X., Zhang, L. & Zeng, X. 2018a Vapor-liquid interfacial reaction to fabricate superhydrophilic and underwater superoleophobic thiol-ene/silica hybrid decorated fabric for oil/water separation. *Applied Surface Science* **427**, 92–101.

Li, J., Bai, X., Tang, X., Zha, F., Feng, H. & Qi, W. 2018b Underwater superoleophobic/underoil superhydrophobic corn cob coated meshes for on-demand oil/water separation. *Separation and Purification Technology* **195**, 232–237.

Li, J., Long, Y., Xu, C., Tian, H., Wu, Y. & Zha, F. 2018c Continuous, high-flux and efficient oil/water separation assisted by an integrated system with opposite wettability. *Applied Surface Science* **433**, 374–380.

Li, X., Shan, H., Zhang, W. & Li, B. 2020 3D printed robust superhydrophilic and underwater superoleophobic composite membrane for high efficient oil/water separation. *Separation and Purification Technology* **237**, 116324.

Lian, Z., Xu, J., Wang, Z., Yu, Z., Weng, Z. & Yu, H. 2018 Nanosecond laser induced underwater superoleophobic and underoil superhydrophobic mesh for oil/water separation. *Langmuir* **34**, 2981–2988.

Liu, P., Niu, L., Tao, X., Li, X., Zhang, Z. & Yu, L. 2018a Preparation of superhydrophobic-oleophilic quartz sand filter and its application in oil-water separation. *Applied Surface Science* **447**, 656–663.

Liu, J., Zhu, X., Zhang, H., Wu, F., Wei, B. & Chang, Q. 2018b Superhydrophobic coating on quartz sand filter media for oily wastewater filtration. *Colloids and Surfaces A: Physicochemical and Engineering Aspects* **553**, 509–514.

Meng, W., Li, P., Lan, Y., Shi, X., Peng, S., Qu, H. & Xu, J. 2020 Green fabrication of superhydrophilic and underwater superoleophobic coatings with applications in oil-water separation, photocatalysis and fire-retardance. *Separation and Purification Technology* **233**, 115988.

Michielsen, S. & Lee, H. J. 2007 Design of a superhydrophobic surface using woven structures. *Langmuir* **23**, 6004–6010.

Milionis, A., Loth, E. & Bayer, I. S. 2016 Recent advances in the mechanical durability of superhydrophobic materials. *Advances in Colloid and Interface Science* **229**, 57–79.

Milne, A., Elliott, J., Zabeti, P., Zhou, J. & Amirfazli, A. 2011 Model and experimental studies for contact angles of surfactant solutions on rough and smooth hydrophobic surfaces. *Physical Chemistry Chemical Physics* **13**, 16208–16219.

Moosai, R. & Dawe, R. A. 2003 Gas attachment of oil droplets for gas flotation for oily wastewater cleanup. *Separation & Purification Technology* **33**, 303–314.

Obaid, M., Mohamed, H. O., Yasin, A. S., Yassin, M. A., Fadali, O. A., Kim, H. & Barakat, N. A. M. 2017 Under-oil superhydrophilic wetted PVDF electrospun modified membrane for continuous gravitational oil/water separation with outstanding flux. *Water Research* **123**, 524–535.

Pintor, A. M. A., Vilar, V. J. P., Botelho, C. M. S. & Rui, A. R. B. 2016 Oil and grease removal from wastewaters: sorption treatment as an alternative to state-of-the-art technologies. A critical review. *Chemical Engineering Journal* **297**, 229–255.

Shang, Q., Chen, J., Liu, C., Hu, Y., Hu, L., Yang, X. & Zhou, Y. 2019 Facile fabrication of environmentally friendly bio-based superhydrophobic surfaces via UV-polymerization for self-cleaning and high efficient oil/water separation. *Progress in Organic Coatings* **137**, 105346.

Shannon, M. A., Bohn, P. W., Elimelech, M., Georgiadis, J. G., Mariñas, B. J. & Mayes, A. M. 2008 Science and technology for water purification in the coming decades. *Nature* **452**, 301.

Song, J., Lu, Y., Luo, J., Huang, S., Wang, L., Xu, W. & Parkin, I. P. 2015 Barrel-shaped oil skimmer designed for collection of oil from spills. *Advanced Materials Interfaces* **2**, 1500350.

Tang, W., Sun, D., Liu, S., Li, B., Sun, W., Fu, J., Li, B., Hu, D. & Yu, J. 2019 One step electrochemical fabricating of the biomimetic graphene skins with superhydrophobicity and superoleophilicity for highly efficient oil-water separation. *Separation and Purification Technology* **236**, 116293.

Tanudjaja, H. J., Hejase, C. A., Tarabara, V. V., Fane, A. G. & Chew, J. W. 2019 Membrane-based separation for oily wastewater: a practical perspective. *Water Research* **156**, 347–365.

Taylor, W. D. 1948 Fundamentals of soil mechanics. *Soil Science* **66**, 161.

Teng, C., Lu, X., Ren, G., Zhu, Y., Wan, M. & Jiang, L. 2014 Underwater self-cleaning PEDOT-PSS hydrogel mesh for effective separation of corrosive and hot oil/water mixtures. *Advanced Materials Interfaces* **1**, 1400099.

Tian, L., Li, W., Ye, H., Zhu, L., Chen, H. & Liu, H. 2019 Environmentally benign development of superhydrophilic and underwater superoleophobic mesh for effective oil/water separation. *Surface and Coatings Technology* **377**, 124892.

Tudu, B. K. & Kumar, A. 2019 Robust and durable superhydrophobic steel and copper meshes for separation of oil-water emulsions. *Progress in Organic Coatings* **133**, 316–324.

Wang, J. & Liu, S. 2020 Fabrication of water-repellent double-layered polydopamine/copper films on mesh with improved abrasion and corrosion resistance by solution-phase reduction for oily wastewater treatment. *Separation and Purification Technology* **233**, 9.

Wang, B., Liang, W., Guo, Z. & Liu, W. 2015 Biomimetic super-lyophobic and super-lyophilic materials applied for oil/water separation: a new strategy beyond nature. *Chemical Society Reviews* **44**, 336.

Wang, Z., Elimelech, M. & Lin, S. 2016 Environmental applications of interfacial materials with special wettability. *Environmental Science & Technology* **50**, 2132–2149.

Yagoub, H., Zhu, L., Shibraen, M. H. M. A., Altam, A. A., Babiker, D. M. D., Rehan, K., Mukwaya, V., Xu, J. & Yang, S. 2019 Manipulating the surface wettability of polysaccharide based complex membrane for oil/water separation. *Carbohydrate Polymers* **225**, 115231.

Yang, R., Moni, P. & Gleason, K. K. 2015 Ultrathin zwitterionic coatings for roughness-independent underwater superoleophobicity and gravity-driven oil–water separation. *Advanced Materials Interfaces* **2**, 1400489.

Yao, H., Lu, X., Xin, Z., Zhang, H. & Li, X. 2019 A durable bio-based polybenzoxazine/SiO_2 modified fabric with superhydrophobicity and superoleophilicity for oil/water separation. *Separation and Purification Technology* **229**, 115792.

Yin, X., Wang, Z., Shen, Y., Mu, P., Zhu, G. & Li, J. 2020a Facile fabrication of superhydrophobic copper hydroxide coated mesh for effective separation of water-in-oil emulsions. *Separation and Purification Technology* **230**, 115856.

Yin, X., Yu, S., Wang, L., Li, H. & Xiong, W. 2020b Design and preparation of superhydrophobic NiS nanorods on Ni mesh for oil-water separation. *Separation and Purification Technology* **234**, 116126.

Yong, J., Chen, F., Yang, Q., Bian, H., Du, G., Shan, C., Huo, J., Fang, Y. & Hou, X. 2016 Oil-water separation: a gift from the desert. *Advanced Materials Interfaces* **3**, 1500650.

Zang, D., Liu, F., Zhang, M., Niu, X., Gao, Z. & Wang, C. 2015 Superhydrophobic coating on fiberglass cloth for selective removal of oil from water. *Chemical Engineering Journal* **262**, 210–216.

Zaroual, Z., Azzi, M., Saib, N. & Chainet, E. 2006 Contribution to the study of electrocoagulation mechanism in basic textile effluent. *Journal of Hazardous Materials* **131**, 73–78.

Zhang, F., Zhang, W., Shi, Z., Wang, D., Jin, J. & Jiang, L. 2013 Nanowire-haired inorganic membranes with superhydrophilicity and underwater ultralow adhesive superoleophobicity for high-efficiency oil/water separation. *Advanced Materials* **25**, 4192–4198.

Zhang, Z., Luo, X., Liu, Y., Zhou, P., Ma, G., Lei, Z. & Lei, L. 2015 A low cost and highly efficient adsorbent (activated carbon) prepared from waste potato residue. *Journal of the Taiwan Institute of Chemical Engineers* **49**, 206–211.

Zhang, J. C., Liu, J. Y., Wang, G. S., Huang, L., Chen, F. Z. & Liu, X. 2019 Controllable wettability of laser treated aluminum mesh for on-demand oil/water separation. *Journal of Dispersion Science and Technology* **40**, 1627–1636.

Zhou, X., Yu, S., Zang, J., Lv, Z., Liu, E. & Zhao, Y. 2019 Colorful nanostructured TiO_2 film with superhydrophobic–superhydrophilic switchable wettability and anti-fouling property. *Journal of Alloys and Compounds* **798**, 257–266.

First received 9 November 2021; accepted in revised form 3 April 2022. Available online 23 April 2022